Journal of Solid State Chemistry **152,** 21–36 (2000)
doi:10.1006/jssc.2000.8673, available online at http://www.idealibrary.com on IDEAL®

SECTION 2: NEW PERSPECTIVES

Mesostructured Metal Germanium Sulfide and Selenide Materials Based on the Tetrahedral $[Ge_4S_{10}]^{4-}$ and $[Ge_4Se_{10}]^{4-}$ Units: Surfactant Templated Three-Dimensional Disordered Frameworks Perforated with Worm Holes

Michael Wachhold,* K. Kasthuri Rangan,* Ming Lei,† M. F. Thorpe,† Simon J. L. Billinge,† Valeri Petkov,† Joy Heising,* and Mercouri G. Kanatzidis*,[1]

*Department of Chemistry and †Department of Physics and Astronomy and Center for Fundamental Materials Research, Michigan State University, East Lansing, Michigan 48824

The polymerization of $[Ge_4S_{10}]^{4-}$ and $[Ge_4Se_{10}]^{4-}$ unit clusters with the divalent metal ions Zn^{2+}, Cd^{2+}, Hg^{2+}, Ni^{2+}, and Co^{2+} in the presence of various surfactant cations leads to novel mesostructured phases. The surfactants are the quaternary ammonium salts $C_{12}H_{25}NMe_3Br$, $C_{14}H_{29}NMe_3Br$, $C_{16}H_{33}NMe_3Br$, and $C_{18}H_{37}NMe_3Br$, which play the role of templates, helping to assemble a three-dimensional mesostructured metal–germanium chalcogenide framework. These materials are stoichiometric in nature and have the formula of $(R\text{–}NMe_3)_2[MGe_4Q_{10}]$ (Q = S, Se). The local atomic structure was probed by X-ray diffuse scattering and pair distribution function analysis methods and indicates that the adamantane clusters stay intact while the linking metal atoms possess a tetrahedral coordination environment. A model can be derived, from the comparison of measured and simulated X-ray powder diffraction patterns, describing the structure as an amorphous three-dimensional framework consisting of adamantane $[Ge_4Q_{10}]^{4-}$ units that are bridged by tetrahedral coordinated M^{2+} cations. The network structures used in the simulations were derived from corresponding disordered structures developed for amorphous silicon. The frameworks in $(R\text{–}NMe_3)_2[MGe_4Q_{10}]$ are perforated with worm hole-like tunnels, occupied by the surfactant cations, which show no long-range order. This motif is supported by transmission electron microscopy images of these materials. The pore sizes of these channels were estimated to lie in the range of 20–30 Å, depending on the appointed surfactant cation length. The framework wall thickness of ca. 10 Å is thereby independent from the surfactant molecules used. Up to 80% of the surfactant molecules can be removed by thermal degradation under vacuum without loss of mesostructural integrity. Physical, chemical, and spectroscopic properties of these materials are discussed. © 2000 Academic Press

[1]To whom correspondence should be addressed. E-mail: kanatzid@cem.msu.edu.

INTRODUCTION

Microporous and mesoporous materials based on elements other than oxide are now of great interest (1, 2), particularly classes of material based on metal chalcogenide frameworks. The combination of nano- and mesoporosity with the unique properties of metal chalogenides such as catalysis (3), semiconductivity (4), and photoconductivity (5) could result in new types of multifunctional materials. For example, it is well known that the reactivity of semiconductor surfaces toward small molecules can be controlled by both light and electrical bias (6). It would be particularly interesting if one could combine, in one material, the shape selectivity of a microporous oxide with the electrical, electronic, and photonic characteristics of a semiconductor (1). Such an accomplishment will permit the exploration of the relatively new concept of catalysis in microporous semiconductors. Various microstructured metal sulfides with open framework topologies resembling those of zeolites have been anticipated (7) and important first steps have been made in recent years. These include $(Me_4N)GeS_x$ (8), $(Me_4N)_2MnGe_4S_{10}$ (9), $(C_6H_{14}N_2)MnGe_4S_{10}\cdot 3H_2O$ (10), $[(C_6H_{13}N_2)_2(H_2O)][AgGe_4S_{10}]$ (11), $(Me_4N)_2FeGe_4S_{10}$ (12), and the dimetal linked framework $(Me_4N)_2(Ag,Cu)_2Ge_4S_{10}$ (13), the open framework structures of $(Me_4N)[Sb_3S_5]$ (2a), $(Ph_4P)[In(Se_6)_2]$ (14), $K_2[PdSe_{10}]$ (15), $\{(CH_3)N(CH_2CH_2)_3N\}_2[Pd(Se_6)_2]$ (16), $(H_3NCH_2CH_2NH_2)_2[Pd(Se_5)_2]$ (16), and $K_2[(H_3NCH_2CH_2NH_3)_2\text{-}[Pd(Se_4)_2\cdot 2Se_4]$ (16); the various alkylammonium salts of $[Sn_3Q_7]^{2-}$ (17, 18) (Q = S, Se), $(Pr_4N)_2Sn_4S_9$, (19, 20), $Cs_2Sn_3S_7\cdot\frac{1}{2}S_8$ (21), KBi_3S_5 (22), and $(Et_4N)_4[Hg_7Se_9]$ (23), among others (24). The adsorption and sensing behavior of some structurally well-defined microporous layered tin sulfides, $(cation)_2Sn_3S_7$, have been explored (25). Small

0022-4596/00 $35.00

molecules such as NH_3, H_2S, and alcohols were found to interact with these materials. Electrical and optical responses with respect to adsorption of specific guests showed high sensitivity, reversibility, and fast reaction times that are comparable to those of some commercial semiconductor sensors. This suggests that microporous metal sulfides may be potentially useful in environmental, industrial, and biomedical monitoring.

On a parallel track, the dramatic advances in the synthesis of *mesostructured* silicates and aluminosilicates in the last 5 years have generated great excitement (26, 27). The enormous success achieved in constructing silicates and aluminosilicates of virtually any pore size begs the question of whether sulfidic and other nonoxidic mesoporous analogs could similarly be made. Direct analogs of silicate materials, of course, would be the thiosilicates and thioaluminosilicates. However, these systems are expected to be very unstable to hydrolysis. Therefore, one needs a working analog for the sulfides that would mimic some of the characteristics of the $[SiO_4]^{4-}$ unit. A suitable such building unit with tetrahedral topology and similar charge is the adamantane thioanion $[Ge_4S_{10}]^{4-}$ (or its selenium analog), which is made of four corner-linked $[GeS_4]^{4-}$ tetrahedra; see Fig. 1. These adamantane clusters are stable in water over a wide pH range (28) and are therefore well suited for ion-exchange or self-assembly-type reactions with metal ions and water-soluble cationic templates. Because they can serve as precursors for the construction of micro- and mesoporous sulfidic phases, we have already studied in detail their corresponding salts with various surfactants (29). Namely, we have reported the single-crystal structures of the lamellar $(R\text{–}NMe_3)_4Ge_4S_{10}$ compounds ($R = n$-$C_{12}H_{25}$, n-$C_{14}H_{29}$, n-$C_{16}H_{33}$, and n-$C_{18}H_{37}$) and their physicochemical behavior under a variety of conditions.

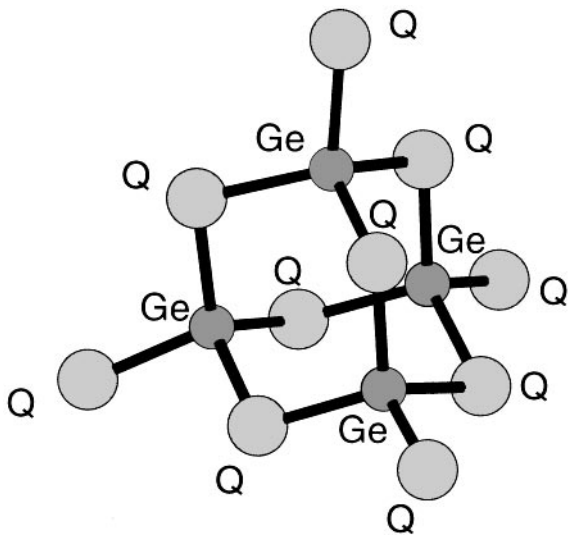

FIG. 1. Structure of the adamantane $[Ge_4Q_{10}]^{4-}$ building block

Recently, the preparation of δ-GeS_2, a new, open framework form of germanium disulfide, generated from the acid polymerization of $[Ge_4S_{10}]^{4-}$ units was reported, adding support to the notion that the germanium sulfide cluster can serve as a functional analog of $[SiO_4]^{4-}$ (30).

Already reports on mesostructured chalcogenides have begun to appear. Recently, mesostructured CdS (31), CdSe (32), and ZnS (33) prepared through the incorporation of cationic and neutral surfactants have been reported. Also, initial studies on mesostructured tin sulfides (34) have been carried out (35). A brief report on the synthesis of mesostructured thiogermanates resulting from the hydrothermal treatment of amorphous GeS_2 and acetyltrimethylammonium bromide is also noteworthy (36).

Our approach toward achieving microporous and mesoporous materials is twofold. One methodology aims at pillaring various metal dichalcogenides with appropriate metal–chalcogenide clusters (37). The second approach, described here, involves the liquid crystal template method now used to prepare mesoporous silicate and aluminosilicate molecular sieves. We have explored the use of the electrostatic self-assembly approach, developed at Mobil (26), using a mainly aqueous route (with methanol or ethanol added) and employing suitable cationic organic surfactant species, to form mesoporous metal sulfide frameworks. Here we report initial results of a study regarding mesostructured metal germanium sulfides using electrostatic self-assembly in which we have polymerized $[Ge_4Q_{10}]^{4-}$ units ($Q = S, Se$) with a variety of divalent transition metal ions (i.e., Zn^{2+}, Cd^{2+}, Hg^{2+}, Ni^{2+}, and Co^{2+}) in the presence of the surfactant templates $C_{12}H_{25}NMe_3Br$, $C_{14}H_{29}NMe_3Br$, $C_{16}H_{33}NMe_3Br$, and $C_{18}H_{37}NMe_3Br$. We describe a new class of mesostructured metal/Ge_4Q_{10} based frameworks with large, worm-hole surfactant-filled tunnels.

Recently, a report appeared on the nonaqueous supramolecular assembly of mesostructured metal germanium sulfides from $[Ge_4S_{10}]^{4-}$ clusters (38). These materials contain CTA surfactant (i.e., $C_{16}H_{33}NMe_3^+$) and $M^{\parallel}_2Ge_4S_{10}$ frameworks and are claimed to contain hexagonally packed pores ($M^{\parallel} = Zn^{2+}$, Ni^{2+}, Cu^+, and Co^{2+}). These phases require formamide as the synthesis solvent with water molecules ($\sim$5 wt%) of solvation. The materials described here seem to differ both qualitatively and quantitatively from the CTA/$M_2Ge_4S_{10}$ systems (38). These differences include (a) synthesis method, (b) chemical formula (c) overall three-dimensional framework organization, and (d) thermal stability.

EXPERIMENTAL SECTION

Reagents

Chemicals were used as obtained: (i) germanium powder, 99.999% purity, -100 mesh, Alfa Aesar; (ii) sulfur powder,

sublimed, J. T. Baker Chemical Co.; (iii) selenium powder; (iv) sodium metal, 98%, Spectrum Chemical; (v) potassium metal; (vi) various metal chlorides ($ZnCl_2$, $CdCl_2$, $HgCl_2$, $CoCl_2 \cdot 6H_2O$, $NiCl_2 \cdot 6H_2O$); (vii) dodecyltrimethylammonium bromide ($C_{12}Br$), 99%, TCI America; (viii) tetradecyltrimethylammonium bromide ($C_{14}Br$), 99%, Aldrich Chemical; (ix) hexadecyltrimethylammonium bromide ($C_{16}Br$), 98%, Alfa Avocado; (x) octadecyltrimethylammonium bromide ($C_{18}Br$), Fluka Chemika; (xi) methanol, ethanol ACS anhydrous, EM Science, Inc., (xii) diethyl ether, ACS anhydrous, EM Science, Inc.; (xiii) acetone, ACS anhydrous, EM Science, Inc.

Synthesis of $Na_4Ge_4S_{10}$

This compound was prepared by heating stoichiometric amounts of thoroughly mixed Na_2S, Ge, and S (1 : 2 : 4) in evacuated quartz tubes at 850°C for 48 h (29). This procedure gave a very hygroscopic, pale-yellow crystalline translucent phase that was stored in a nitrogen-filled glove box.

Synthesis of $K_4Ge_4Se_{10}$

K_2Se was prepared by reacting stoichiometric amounts of the elements in liquid ammonia. $K_4Ge_4Se_{10}$ was prepared by heating stoichiometric amounts of thoroughly mixed K_2Se, Ge, and Se (1 : 2 : 4) in evacuated quartz ampoules at 850°C for 32 h. This procedure gave an air-sensitive, shiny yellow powder, which was stored in a nitrogen-filled glove box.

Preparation of $(R\text{–}NMe_3)_2[MGe_4S_{10}]$ (M = Co, Ni, Zn, Cd, Hg)

$(R\text{–}NMe_3)_2[MGe_4S_{10}]$ phases were prepared in ethanol/H_2O (5 : 1 by volume) solutions at room temperature; the surfactants (1 mmol) were dissolved in 200 mL of ethanol/H_2O solution at room temperature. $Na_4Ge_4S_{10}$ (0.35g, 0.5 mmol) was dissolved in 20 mL of distilled water by stirring and a small amount of insoluble impurities was removed by filtration. MCl_2 (0.5 mmol) was dissolved in 20 mL of distilled water and the $Na_4Ge_4S_{10}$ and MCl_2 solutions were added simultaneously to the surfactant solution under constant stirring to form copious precipitate. The mixture was stirred for 3 h at room temperature, then filtered, washed with water, and vacuum dried overnight. The yields of the colorless (Zn, Cd), yellow (Hg), yellow-brownish (Ni), or green (Co) precipitates is typically 50% in all cases, based on $Na_4Ge_4S_{10}$. Elemental analyses coupled with thermal gravimetric analyses were reproducible and consistent with the chemical formula $(R\text{–}NMe_3)_2[MGe_4Se_{10}]$.

Preparation of $(R\text{–}NMe_3)_2[MGe_4Se_{10}]$ (M = Zn, Cd, Hg, Co, Ni)

Method a. Method a is a 1 : 1 reaction of lamellar $(R\text{–}NMe_3)_4Ge_4Se_{10}$ phases (29) with metal chlorides ($ZnCl_2$, $CdCl_2$, $HgCl_2$, $CoCl_2 \cdot 6H_2O$, $NiCl_2 \cdot 6H_2O$). The $(R\text{–}NMe_3)_4Ge_4Se_{10}$ phases are accessible through a stoichiometric reaction of $K_4Ge_4Se_{10}$ and $(R\text{–}NMe_3)Br$. The procedures are similar to the synthesis of the corresponding sulfur phases described elsewhere (29). $(R\text{–}NMe_3)_4Ge_4Se_{10}$ is dissolved in a warm ($\sim$60–80°C) 1 : 1 ethanol/water mixture ($\sim$20–50 ml). A solution of MCl_2 in ethanol/water mixture is then added dropwise to the stirred $(R\text{–}NMe_3)_4Ge_4Se_{10}$ solution to give instantly a yellow (Zn, Cd) or yellow-brownish (Hg, Co, Ni) precipitate. The resulting suspension was stirred overnight for the Zn and Cd compounds or for about 1 h for Hg, Co, and Ni. The compounds were isolated by centrifugation and subsequent decanting of the solvent. Each product was washed with water and acetone to remove all residues of the $(R\text{–}NMe_3)Cl$ salt and dried with diethyl ether. The yield is typically >90%, indicating a nearly quantitative reaction. Elemental analyses coupled with thermal gravimetric analyses indicated the formula $(R\text{–}NMe_3)_2[MGe_4Se_{10}]$.

Method b. Method b is a direct reaction of the precursor $K_4Ge_4Se_{10}$ with surfactant and metal chloride. $K_4Ge_4Se_{10}$ and two equivalents of the surfactant salt $(R\text{–}NMe_3)Br$ were dissolved in a 1 : 1 mixture of H_2O/MeOH ($\sim$20 ml) in an Erlenmeyer flask and heated to 60–80°C, giving a yellow solution for $C_{12}Br$ and $C_{14}Br$. For $C_{16}Br$ and $C_{18}Br$, acetone was also added to ensure complete dissolution. A solution of the MCl_2 salt in 10 mL H_2O was slowly added to this mixture under vigorous stirring, leading to immediate precipitation of the product. The process of isolation and purification was the same as that for Method a. From this point forward these materials are designated C_nMGeQ (n = 12, 14, 16, and 18; M = Zn, Cd, Hg, Co, Ni; Q = S, Se).

Physical Measurements

Powder X-ray diffraction. Analyses were performed using a computer-controlled INEL CPS120 powder diffractometer in asymmetric reflection mode, operating at 40 kV/20 mA, with a graphite monochromatized Cu$K\alpha$ radiation. The diffractometer was calibrated in the low-angle region using hexadecyltrimethylammonium bromide ($C_{16}Br$) as external standard.

The X-ray diffraction data for the pair distribution function determination were collected independently using a Huber diffractometer in symmetric reflection geometry (out to $2\theta_{max}$ of 140°) and Mo$K\alpha$ radiation (λ = 0.7107 Å). The pair distribution function (PDF) was obtained using standard methods (39). The data were corrected for

background, absorption, polarization, and Compton and multiple scattering and normalized by the incident flux, the number of scatterers, and the average atomic form factor of the sample to obtain the normalized total scattering function $S(Q)$ ($Q = 4\pi \sin(\theta)/\lambda$, where 2θ is the scattering angle) (10). The reduced radial distribution function, or PDF, $G(r)$, is obtained from $S(Q)$ through the Fourier transform

$$G(r) = 4\pi r[\rho(r) - \rho_0] = \frac{2}{\pi}\int_0^\infty Q[S(Q) - 1]\sin(Qr)dQ, \quad [1]$$

where $\rho(r)$ is atomic pair density function and ρ_0 is the average number density. The function $G(r)$ has the property that peaks occur in the function at distances, r, which separate pairs of atoms in the solid. For example, the first strong peak occurs at $r \sim 2.2$ Å corresponding to the Ge–S nearest neighbor peak in these materials. It is a measure of the short-range atomic order in the solid and does not presume any crystallinity (41, 42).

Infrared and Raman spectroscopy. Infrared spectra, in the IR region (6000–400 cm^{-1}) on far-IR region (600–100 cm^{-1}), were recorded with a computer-controlled Nicolet 750 Magna-IR Series II spectrometer equipped with a TGS/PE detector and a silicon beam splitter in 2 cm^{-1} resolution. The samples were mixed with ground dry CsI and pressed into translucent pellets. Raman spectra of the C_nMGeQ powders were recorded on a Holoprobe Raman spectrograph equipped with a 633-nm helium–neon laser and a CCD camera detector. The instrument was coupled to an Olympus BX60 microscope. The spot size of the laser beam was 10 mm when a 50× objective lens was used.

Solid state UV/Vis/near IR spectroscopy. UV/vis/near IR diffuse reflectance spectra were obtained at room temperature on a Shimadzu UV-3101PC double-beam, double monochromator spectrophotometer in the wavelength range of 200–2500 nm. The instrument is equipped with an integrating sphere and controlled by a PC. $BaSO_4$ powder was used as a reference (100% reflectance) and base material on which the ground powder sample was coated. Reflectance data were converted to absorbance data as described elsewhere (43). The band gap energy value was determined by extrapolation from the linear portion of the absorption edge in a (α/S) versus E plot.

Thermogravimetric analyses (TGA). TGA data were obtained with a computer-controlled Shimadzu TGA-50 thermal analyzer. Typically 25 mg of sample was placed in a quartz bucket and heated in a nitrogen flow of 50 ml/min with a rate between 2 and 10°C/min. The residues from the TGA experiments were examined by X-ray powder diffraction.

Differential scanning calorimetry (DSC). DSC experiments were performed on a computer-controlled Shimadzu DSC-50 thermal analyzer. About 10 mg of samples was sealed under nitrogen in an aluminum container. An empty container was used as a reference. All measurements were done with a heating rate of 2°C/min.

Semiquantitative microprobe analyses (EDS). The analyses were performed using a JEOL JSM-35C scanning electron microscope (SEM) equipped with a Tractor Northern energy dispersive spectroscopy (EDS) detector. Data acquisition was performed several times in different areas of the samples using an accelerating voltage of 20 kV and 30–35 s accumulation time.

Transmission electron microscopy (TEM). High-resolution transmission electronmicrographs were acquired with a JEOL 120CX instrument equipped with a CeB_6 filament and operating at 120 kV. A carbon-supported copper grid was dipped in the dry powder or in a suspension of the sample in hexane.

RESULTS AND DISCUSSION

Self-Assembly and Chracterization of Mesostructured $(R\text{–}NMe_3)_2[MGe_4Q_{10}]$ Phases (Q = S, Se; M = Zn, Cd, Hg, Co, Ni)

Syntheses. Using metathesis reactions between the $[Ge_4Q_{10}]^{4-}$ cluster anions and the metal dichlorides in the presence of long-chain cationic surfactant molecules, we were able to synthesize a number of C_nMGeQ (n = 12, 14, 16, 18) compounds with various divalent metal ions such as Zn, Cd, Hg, Ni, or Co (44). The solvent medium employed was a mixture of water/methanol or water/ethanol. The reactions can be performed at room temperature or in warm solvent mixture, either by mixing the C_nGeQ and MCl_2, or $A_4Ge_4Q_{10}$ (A = Na, K) with MCl_2 salts and $C_nH_{2n+1}NMe_3Br$, see Eqs. [2] and [3]. In all cases mixing of the reactant solutions lead to an immediate precipitation of the products. The sulfide phases are white (Zn and Cd) or yellow (Hg), whereas the selenide phases are generally darker in color (yellow for Zn, Cd, brownish for Hg). On the other hand, the Co phases are dark green (S) or brownish black (Se). The products C_nMGeQ are insoluble in all common solvents e.g. H_2O, alcohols or acetone. The composition of these materials, as determined from elemental analysis, is reproducible and consistent with the formula $(R\text{–}NMe_3)_2[MGe_4Q_{10}]$, indicating that these are well defined stoichiometric compounds in which the charge on the $[Ge_4Q_{10}]^{4-}$ cluster is balanced by one M^{2+} and two surfactant $R\text{–}NMe_3^+$ ions. In fact, the same composition is obtained regardless of the $[Ge_4Q_{10}]^{4-}/MCl_2$ ratio.

Interestingly, the conditions used to obtain C_nMGeQ did not yield the corresponding phases with Mn^{2+} ions (45).

$$(R\text{–}NMe_3)_4Ge_4Se_{10} + MCl_2 \rightarrow (R\text{–}NMe_3)_2[MGe_4Se_{10}] + 2(R\text{–}NMe_3)Cl \quad [2]$$

$$2C_nH_{2n+1}N(CH_3)_3Br + Na_4Ge_4Q_{10} + MCl_2 \rightarrow [C_nH_{2n+1}N(CH_3)_3]_2MGe_4Q_{10} + 2NaBr + 2NaCl \quad (Q = S, Se) \quad [3]$$

It comes as a surprise to us that the formamide-made materials described by Ozin *et al.* (38) seem to have a different stoichiometry, namely, $(C_{16}H_{33}NMe_3)_2\,M_2Ge_4S_{10}$ (when $M = Zn$, Ni) and $(C_{16}H_{33}NMe_3)_2\,M_4Ge_4S_{10}$ (when $M = Cu$). These formulas imply the presence of reduced metal ions such as Zn^{1+} and Ni^{1+} (or $Zn^{2+/0}$ and $Ni^{2+/0}$ couples) and Cu^0.

Structural Chracterization

The most important question to be posed here is what is the structure of the C_nMGeQ phases? Particularly we are interested in the shape and type of the anionic $[MGe_4Q_{10}]^{2-}$ framework. To address this issue we combine the results of a large variety of experimental techniques including X-ray scattering, transmission electron microscopy, infrared and Raman spectroscopy, and thermal analysis. Structural characterization was carried out using low- and high-angle X-ray diffraction and PDF analysis. The data have been compared to theoretical mesostructured framework models that capture the essence of their open three-dimensional architecture.

Low-angle diffraction. All phases exhibit a very strong and relatively sharp peak in the low-angle region. Figure 2 shows a typical X-ray diffraction pattern from the mesostructured phase C_{14}ZnGeS prepared according to the synthesis described above. Figures 3a–3d show the low–angle portion of typical powder patterns for C_nMGeS and C_nMGeSe (M = Zn and Cd) for $n = 12$, 14, 16, and 18. Such a low-angle diffraction peak implies the presence of structures on the mesoscopic scale in the sample. The d-spacing of such a peak indicates the average separation of mesoscopic features such as the pore–pore separation in a mesoporous material. For example, similar peaks are observed in many mesostructured silicates, aluminophosphates, and other metal oxides where the d-spacing reveals the average mesopore separation (46). In these materials, higher order

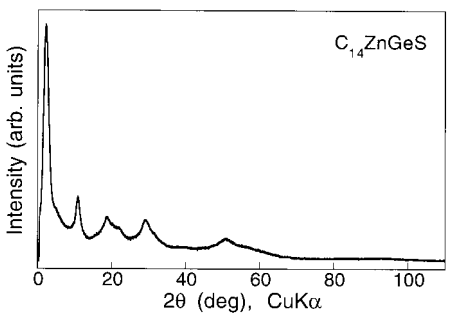

FIG. 2. Typical X-ray diffraction pattern for mesostructured C_nZnGeS.

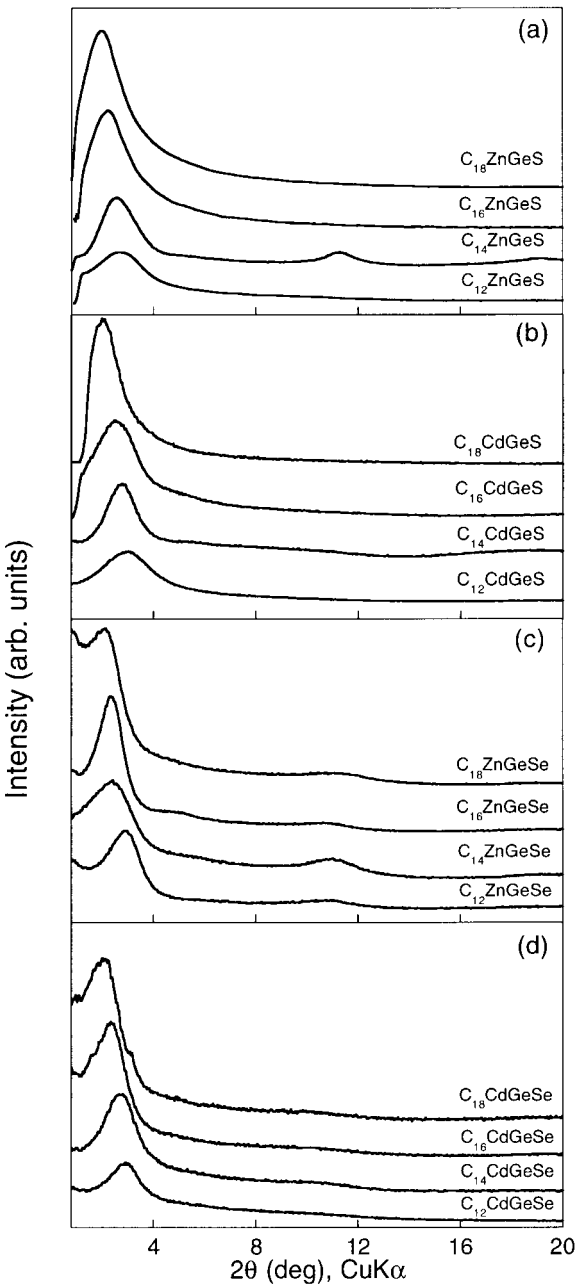

FIG. 3. Low-angle powder X-ray diffraction patterns of (a) C_nZnGeS (b) C_nCdGeS, (c) C_nZnGeSe, and (d) C_nCdGeSe, for $n = 12$, 14, 16, 18 ($0 < 2\theta < 20°$); the d spacing is almost linearly dependent of the surfactant chain in all cases, see Fig. 4.

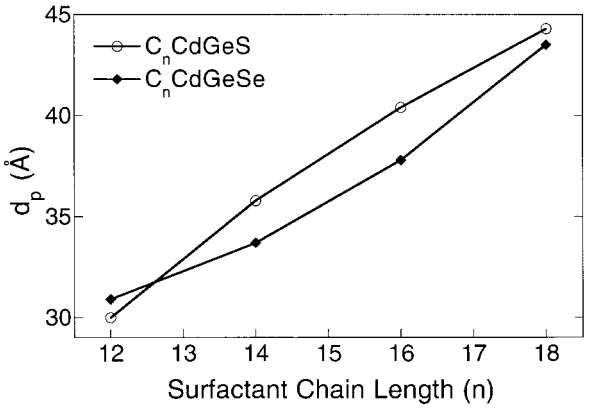

FIG. 4. Average pore spacing d_p as a function of surfactant chin length.

reflections are often observed indicating that the pores form a regular hexagonal packing arrangement or a well-ordered lamellar structure. Higher order reflections (e.g., 110 and 200) were also reportedly observed in the formamide-assembled $C_{16}H_{33}NMe_3/MGeS_{10}$ systems. In contrast, the C_nMGeS and C_nMGeSe materials, which form essentially in an aqueous medium, do not show such reflections, suggesting the absence of regular pore packing with intermediate range order (47, 48). Apparently, the choice of solvent seems to affect both the stoichiometry as well as the topology of the mesostructure. The upturn in the scattering intensity below the first low-angle peak in each data set may indicate the presence of pronounced small-angle scattering, another indication that there are density inhomogeneities (i.e., mesoscopic structural features) on the nanometer–micron length scale.

The *d*-spacing of the low-angle peak (denoted d_p since it presumably yields the pore separation) in the C_nMGeQ samples increases with an increase in surfactant chain length and lies between $\sim$30 Å for C_{12} and $>$40 Å for C_{18} surfactants. This systematic dependence is summarized in Fig. 4 and Table 1.

Wide-angle diffraction. As with other mesostructured materials (e.g., silicate based), the C_nMGeQ products show no long-range order, as seen from the lack of further sharp Bragg diffraction peaks in the powder XRD pattern. This means that the "walls" made from the $[MGe_4Q_{10}]^{2-}$ framework also lack long-range order. However, these materials exhibit well-defined diffuse scattering (at $2\theta > 6°$) consistent with the presence of short-range local order and nonperiodic wall structure much like the wall structure of MCM-41 or MSU-3 albeit with greater intensity due to the heavier elements involved (49). The wide-angle scattering data are shown in Figs. 5a–5c. The diffuse scattering pattern is well reproduced on changing the length of the surfactant molecule (Figs. 5a and 5b) and remains qualitatively similar on changing the metal bridging ion (compare Fig. 5a with Fig. 5b). This suggests that the local structure adopted by the transition metal is similar in all phases and that the diffuse scattering is coming predominantly from the adamantoid $[Ge_4Se_{10}]^{4-}$ itself. In the corresponding sulfides, C_nMGeS (compare Figs. 5a and 5b to Fig. 5c), the diffuse

TABLE 1
Summary of the d_p Values for C_nZnGeS, $C_nZnGeSe$, C_nCdGeS, and $C_nCdGeSe$ (n = 12, 14, 16, 18)

	d_p Values [Å]			
Compound	C_{12}	C_{14}	C_{16}	C_{18}
C_nZnGeS	32.7	35.2	42.1	44.0
$C_nZnGeSe$	30.5	36.3	37.8	41.3
C_nCdGeS	30.0	35.8	40.4	44.3
$C_nCdGeSe$	30.9	33.7	37.8	43.5

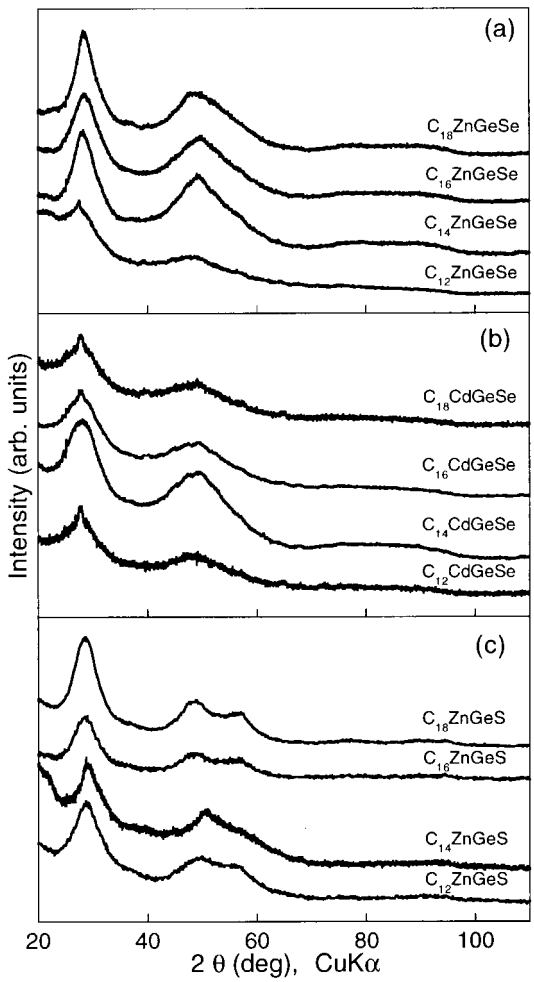

FIG. 5. Wide-angle X-ray diffraction patterns for (a) $C_nZnGeSe$, (b) $C_nCdGeSe$, and (c) C_nZnGeS. The structural parameters used for the calculations are given in Ref. (54).

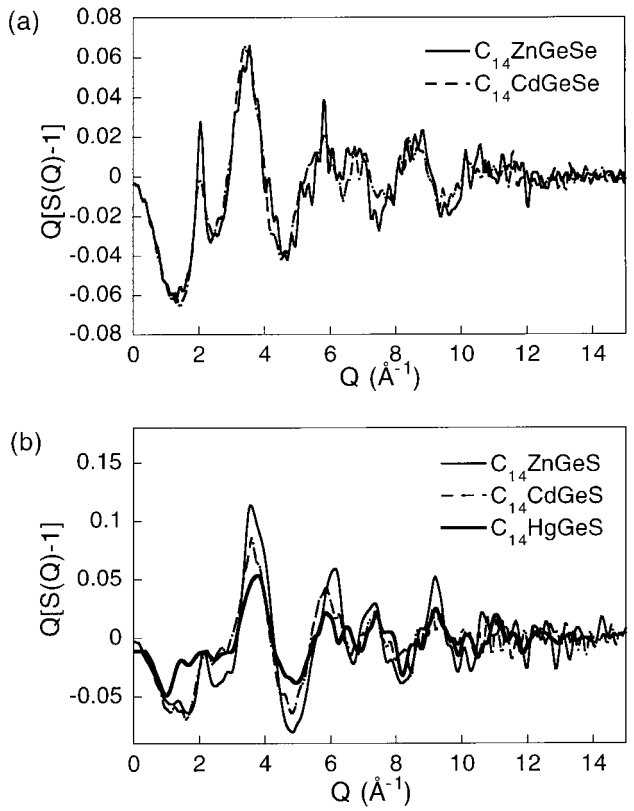

FIG. 6. Reduced structure factors $Q[S(Q) - 1]$ for (a) Se- and (b) S-containing adamantane units (Zn-containing samples, thin solid line; Cd-containing samples, broken line with symbols; Hg-containing sample, thick solid line).

scattering pattern changes, though it still resembles that obtained from the Se analogs. Again, this supports the idea that the diffuse scattering originates primarily from the rigid adamantane molecules.

The atomic PDFs obtained from the wide-angle scattering support this interpretation. Typical reduced structure factors $S(Q)$ obtained from the powder diffraction data are shown in Figs. 6a and 6b. The corresponding PDFs are shown in Figs. 7a and 7b. The PDFs show that the short-range order is well defined as is attested by the presence of interatomic correlation vectors at 2.2 and 3.8 Å which correspond to Ge–S and Ge–Ge distances in the $[Ge_4S_{10}]^{4-}$ cluster. The structural origin of these features is consistent with the presence of adamantane $[MGe_4S_{10}]^{2-}$ building blocks as we describe later. The assignment of characteristic atom-pairs to the strong features in the PDF for the C_{14}ZnGeQ phases is shown in Fig. 7. However, the structural coherence is virtually gone by 10 Å, which is approximately the M–M separation. This suggests that long-range order is destroyed because there is no well-defined orientational relationship between neighboring adamantoid ions, although the metal ions connecting the adamantoid clusters have local tetrahedral geometry and are acting as hinges (see Fig. 8). Details of the structural modeling studies are reported elsewhere (50).

Why C_nMGeQ are not lamellar or one-dimensional. The overall structure of the $[MGe_4Q_{10}]^{2-}$ framework in the C_nMGeQ phases is unlikely to be one- or two-dimensional because the position and intensity of the low-angle peak in the XRD pattern are insensitive to temperature. In one- and two-dimensional systems, large changes are observed in the low-angle diffraction peak as a function of temperature. This is because of large changes in the surfactant chain conformation (liquid crystal type of transition such as disorder, "melting," etc), which causes large movements in the layer or chain spacings of the layers, or due to layer or chain collapse. The high d-spacing peaks of all C_nMGeQ phases move only very little with temperature and survive even after the material has lost most of its surfactant between 200 and 240°C (see below). DSC does not show any phase transitions of the type typically observed in lamellar phases and arises from the "melting" or rearrangement of the long surfactant chains in the intralamellar space. By comparison, the precursor phases C_nGeQ which are lamellar exhibit prominent temperature induced transitions in the range of

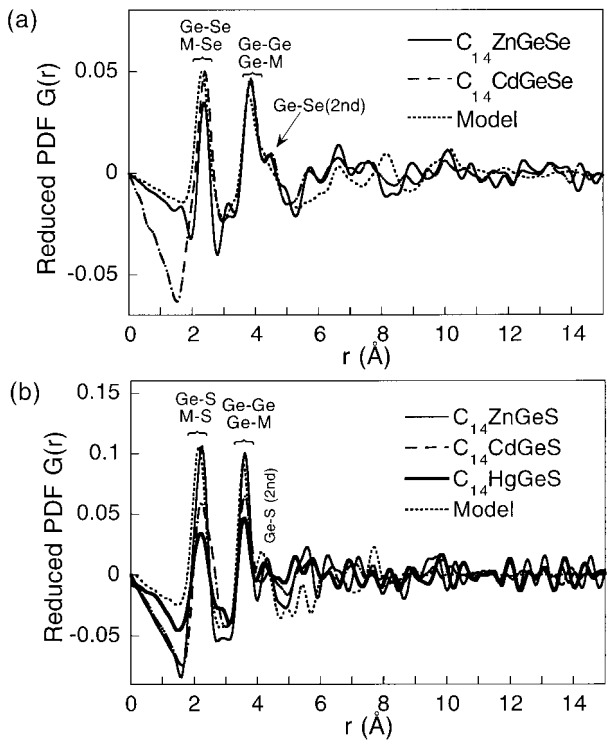

FIG. 7. Reduced radial distribution functions $G(r)$ for (a) Se- and (b) S-containing adamantane units. (Zn-containing samples, thin solid line; Cd-containing samples, broken line with symbols; Hg-containing sample, thick solid line; model calculations, dotted line). These are the Fourier transforms of the data shown in Fig. 6. See text for details.

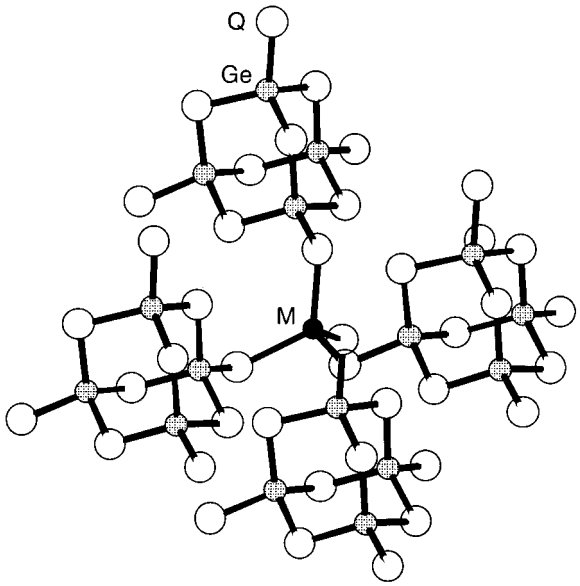

FIG. 8. The building block for an amorphous, three-dimensional framework $^{3}_{\infty}[M\mathrm{Ge}_4Q_{10}]^{2-}$ consisting of tetrahedral coordinated metal center M^{2+} (Zn, Cd, Hg, Co) and adamantane units $[\mathrm{Ge}_4Q_{10}]^{4-}$ (Q = S, Se).

120–160°C. This strongly suggests that indeed we are dealing with a rigid three-dimensional mesostructured amorphous framework.

Furthermore, one-dimensional or two-dimensional systems separated by long surfactant chains are subject to swelling in the presence of suitable polar solvents. For example, the "precursor" lamellar phases $C_n\mathrm{Ge}Q$ swell quickly and reversibly upon exposure to *n*-alcohols and *n*-amines. Although we have tried a large number of such solvents (e.g., many *n*-alcohols, *n*-amines, dimethylformamide, acetonitrile, acetone, benzene, nitromethane, etc.) with $C_nM\mathrm{Ge}Q$, absolutely no swelling was observed as judged by the position of the high *d*-spacing peak.

Finally, high-resolution transmission electron (HRTEM) micrographs reveal that the samples have strongly disordered, worm hole-like features (see Fig. 9) that resemble those of disordered mesoporous oxides (48) and nanostructured ZnS (33). The widths of the channels in Fig. 9 are roughly 22–32 Å. The dimensions of the channels and the significant degree of disorder are consistent with the X-ray powder diffraction results.

A reasonable structural model for these materials is micelle-like ordering of the surfactant chains within the tunnels, with the methyl groups contacting the chalcogenide atoms of the adamantane units. This kind of organic–inorganic contact has already been observed in the $C_n\mathrm{GeS}$ compounds with various surfactant cations (29). In these phases, short C–H···S contacts of about 2.8 Å to the terminal sulfur atoms can be observed. The surfactant-filled tunnels are then poorly organized or even randomly arranged like worm holes, while at the same time keeping a constant average tunnel-to-tunnel distance to be expressed as a strong low-angle peak in the diffraction pattern. The worm hole in which curved tunnels exist in random arrangements, where is some locations they become parallel

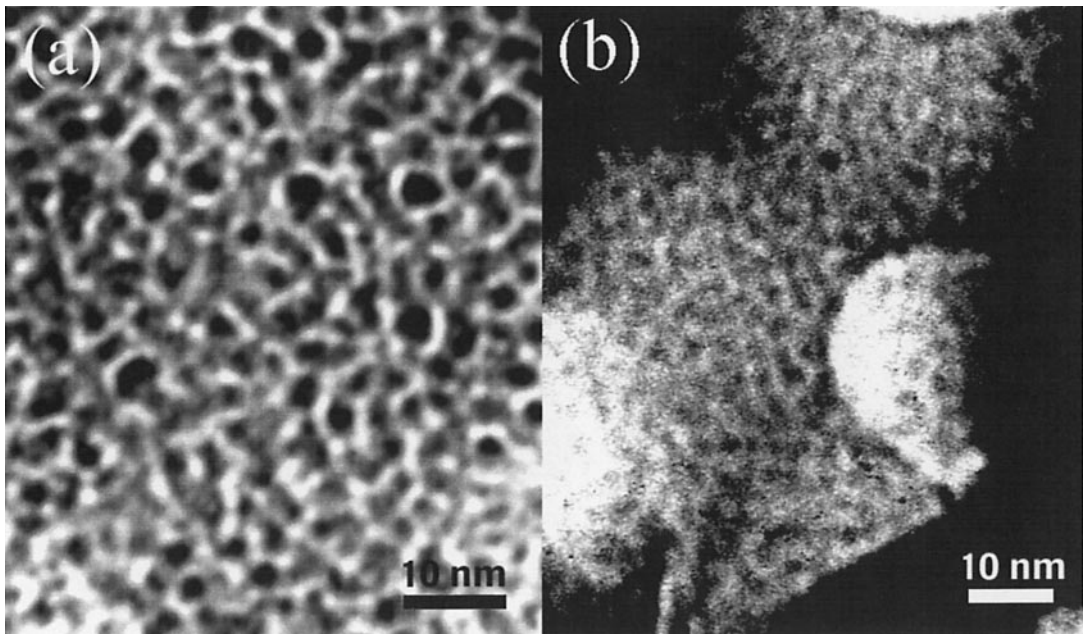

FIG. 9. TEM image of (a) $C_{16}\mathrm{NiGeS}$ and (b) $C_{14}\mathrm{ZnGeSe}$. The surfactant-filled pore space is represented in the white regions.

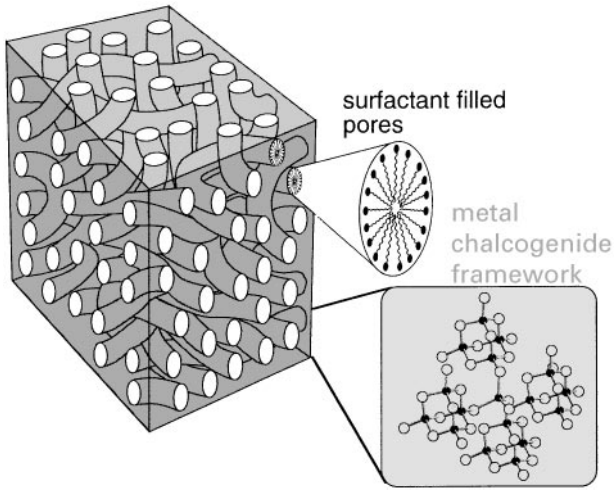

FIG. 10. Proposed structure model of the C_nMGeQ phases. The amorphous $^3_\infty[MGe_4Q_{10}]^{2-}$ framework is perforated by the worm hole-like micelles of surfactant molecules.

while in others they are rather random, much like those in sponges, has been seen already in several types of mesostructured silicas. The HRTEM photographs shown in Fig. 9 are consistent with this description. Therefore, the first strong diffraction peak is due to the semiordered arrangement of surfactant molecules occupying tunnels boring through the three-dimensional $[MGe_4Q_{10}]^{2-}$ frameworks (see Fig. 10). What causes the disordered worm hole arrangement of the holes is probably the very rapid formation deposition of the materials. More ordered frameworks with different morphologies and symmetries may form if the rate of the reaction leading to C_nMGeQ could be slowed down.

Local Order in the $[MGe_4Q_{10}]^{2-}$ Framework and Modeling

All the PDFs discussed above show a well-defined first peak centered at approximately 2.1 Å, a second split peak at approximately 4 Å followed by small oscillations detectable up to $\sim$12 Å. We attempted to model these features to better determine the underlying short-range atomic order. To build models, which capture the structural and diffraction features of C_nMGeQ materials, we used two different and independent approaches. The first uses as a starting point a crystalline analogue, containing adamantane structural unit, and this is used to calculate the PDF (9, 51). From this model structure we were able to assign atomic pairs to each of the peaks in the experimental atomic distribution functions. These assignments are shown in Fig. 7. The intense first peak is due to the first neighbor metal (Zn; Cd; Hg)–(S; Se) and Ge–(S; Se) atomic pairs in the structure. The small hump at approximately 3 Å is due to the first neighbor (S–S) or (Se–Se) atomic pairs in the $[Ge_4Q_{10}]$ unit. The split second peak at 4 Å and its neighbor at 5.5 Å are attributed to the first neighbor (Zn; Ge)–Ge and second neighbor (S; Se)–(S; Se) and Ge–(S; Se) atomic pairs, respectively. The peaks appearing at 6–7 Å are due to Ge–Ge and metal(Zn; Cd; Hg)–Ge second neighbor atomic pairs, and finally, the hardly detectable feature at approximately 9.5–10 Å is attributed to the first neighbor metal (Zn; Cd; Hg)–metal (Zn; Cd; Hg) atomic pairs.

The $G(r)$ function was then calculated based on the crystalline analogue model with some modifications to allow for the lack of long-range order present in the samples. The PDF was calculated using a locally written program, RESPAR, which calculates $G(r)$ from a given crystalline structures (52). Static and thermal disorder is incorporated by broadening PDF peaks with Gaussians. The loss of structural coherence in the present case is modeled by damping $G(r)$ with another broad Gaussian function. As is evident in Fig. 7, the calculated model and the experimental $G(r)$ for $(R\text{-}NMe_3)_2ZnGe_4S_{10}$ agree quite well. The model contains an assembly of well-defined $Ge(Se; S)_4$ units forming $[Ge_4Q_{10}]$ (adamantane-type) blocks that are linked by the respective metal atoms (Zn, Cd, Hg) into a three-dimensional disordered framework. Extensive molecular modeling or three-dimensional MGe_4S_{10} frameworks suggests (53) that the sulfides are more rigid than their selenide analogs. The above studies support the conclusion that $[Ge_4Q_{10}]^{4-}$ molecules are the basic building blocks of these mesostructured materials.

The second approach used to construct a reasonable amorphous $[MGe_4Q_{10}]^{2-}$ framework model, which reproduces the X-ray diffraction properties of C_nMGeQ, involves computer simulations of fully amorphous network structures based on the adamantane molecule. These network structures are derived from corresponding structures developed for amorphous silicon. Calculations performed based on such models (see below) also reproduced the wide-angle scattering, successfully further verifying the notion that the framework is a network of adamantane molecules bridged by metal ions. A good agreement of calculated and measured X-ray scattering patterns, especially for the region between 20° and 30°, was generally achieved with standard bond parameter and angles (54). The M–Q–Ge angles lie between 95° and 130° for a good adjustment of the $2\theta^\circ$ peak.

The intensity, shape and position of all X-ray scattering at $2\theta > 5^\circ$ is generally independent of the nature of the surfactant molecule. By "drilling holes" into the simulated framework structure the low-angle scattering can also be well reproduced. While this is an unphysical and chemically unjustified method of simulating the mesostructure, it does allow the diameter and packing density of possible pores to be simulated and compared to the observed scattering intensity at low angle. For example, in the case of

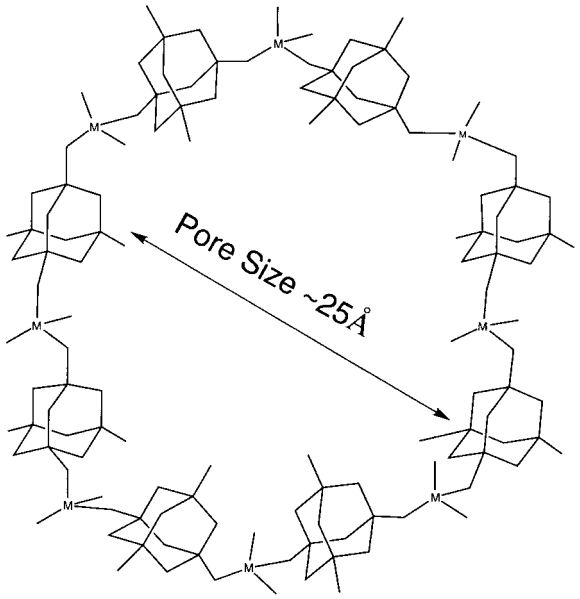

FIG. 11. Schematic model of $[MGe_4Q_{10}]^{2-}$ framework enclosing surfactant micelles.

C_{14}CdGeSe the d_p low-angle peak appears at about 34 Å. In the calculations a reasonable pore diameter of about 24 Å was assumed, giving an average "wall" thickness for the *M*Ge*Q* framework of about 10 Å. Since the position of the low-angle peak correlates very well with the surfactant cation, one can conclude that the wall thickness is constant for all mesostructured materials. This view is consistent with the model, since only the shape of the high-angle area remains unchanged. We estimate that these $[MGe_4Q_{10}]^{2-}$ frameworks are able to enclose a circle with a diameter between 20 and 30 Å using between 6 and 10 stoichiometric units (depending on surfactant) and only changing the relative position to each other but not the connectivities (see Fig. 11).

As the starting point we used a model constructed by Mousseau (55) for amorphous silicon. Mousseau's amorphous silicon model contains 216 atoms in which he deliberately minimized the number of odd numbered rings (4%). Ideally, we would have preferred a structure with no odd rings so that alternate Si sites could be replaced by adamantane and metal ions, respectively (56). Nevertheless, it was possible to come close to this ideal bulk material by using the artifact that when an odd numbered ring appeared a vacancy was left at a random site within the ring. This avoids any adamantane–adamantane or metal–metal neighbors. The adamantane cluster molecules were kept rigid so there are no internal distortions. The structure was then relaxed so that the metal atoms were allowed to move and the adamantane units were allowed the six rigid body motions. This motion was chosen so as to minimize a potential energy

$$E = \frac{\alpha}{2} \sum_{\substack{i=1,\ \text{all metal ions} \\ j=1,\ \text{all 4 neighbors}}} (r_{ij}^2 - r_Z^2)^2 + \frac{\beta_1}{2} \sum_{\substack{i=1,\ \text{all metal ions} \\ 1 \le j < k \le 4}} (\vec{r}_{ij} \cdot \vec{r}_{ik} - \cos\theta_1 r_Z^2)^2 + \frac{\beta_2}{2} \sum_{\substack{i=1\ \text{all sulfurs} \\ j=1,\ k=2}} (\vec{r}_{ij} \cdot \vec{r}_{ik} - \cos\theta_2 r_G r_Z)^2, \quad [4]$$

in which the relative strengths of $\alpha : \beta_1 : \beta_2$ were taken to be $10:5:2$, r_z is the optimum distance from the terminal sulfur atoms to metal atoms, and r_G is the optimum distance between terminal sulfur atoms to the centers of adamantane units. The result is not very sensitive to the values taken, and the values above gave a reasonable fit to experiments as shown in Fig. 12. The first sum is over all the distances between the four terminal S atoms of the $[Ge_4S_{10}]^{4-}$ units that connect to the neighboring metal atoms. The second term is the angle distortion term at the metal atoms, with an assumed optimal angle of 109° for tetrahedral coordination. The last term describes the angular distortion term at the terminal S atoms that bridge to the metal ions with an optimal angle chosen to be 120°. The simulated high-angle X-ray diffraction pattern was in reasonable agreement with that found experimanatally (see Fig. 12). The model is currently being improved by eliminating as many odd rings as possible in the parent amorphous Si structure and by removing parts of the network to form pores into which the organic molecules are placed (57). Preliminary work shows that neither of these two effects changes the computed diffraction pattern at high angles. The full results of the empirical modeling, and computer simulations of the fully amorphous disordered network, are reported elsewhere (50).

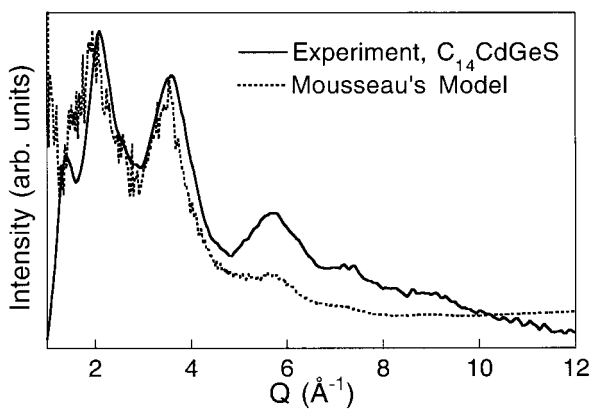

FIG. 12. Experimental and simulated wide-angle X-ray diffraction pattern of C_{14}CdGeS.

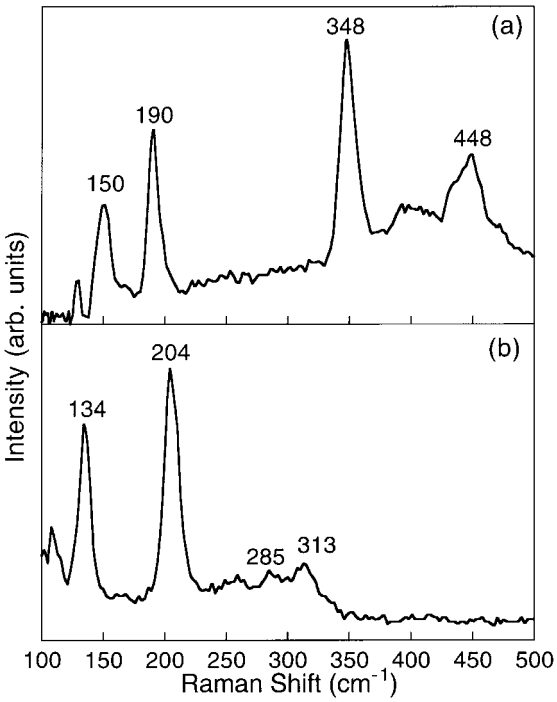

FIG. 13. Raman spectra of (a) C_{18}ZnGeS and (b) C_{16}ZnGeSe.

Raman and Infrared Spectroscopy

The Raman and infrared spectra of all characterized C_nMGeQ phases provide independent and complementary support of the conclusion derived from the PDF scattering analysis presented above. The adamantane cluster remains intact in C_nMGeQ and furthermore the spectra give evidence for additional M–Q bonds of the linkage metal to the terminal chalcogenide ions of the adamantane cluster. The three-dimensional $[MGe_4S_{10}]^{2-}$ framework seems fully bonded judging from the absence of any S–H and Se–H stretching vibrations in the spectra.

Figure 13 shows the Raman spectra of representative members of sulfide and selenide phases in the region 100–500 cm^{-1}. The comparison of these spectra with the corresponding ones of the precursor compounds $A_4Ge_4Q_{10}$ (A = Na, K; Q = S, Se) or C_nGeQ, where the adamantane clusters $[Ge_4Q_{10}]^{4-}$ remain free of linkage metal atoms, shows mainly that the vibration modes of the inner Ge_4Q_6 cage are not substantially affected after bonding to the metal, while the modes involving the terminal chalcogenido atoms are strongly influenced. The fundamental modes of the $[Ge_4Q_{10}]^{4-}$ anion (58) with ideal T_d symmetry belong to the irreducible representations $\Gamma = 3A_1 + 3E + 3T_1 + 6T_2$. Only the A_1, E, and T_2 fundamentals are Raman active, which means that 12 bands should be observable. The three A_1 modes are expected to be the strongest, since they cause large polarizability changes within the cluster. These peaks can easily be assigned at 454, 345, and 189 cm^{-1} in $Na_4Ge_4S_{10}$ and 322, 201.5, and 134 cm^{-1} in $K_4Ge_4Se_{10}$ for modes ν_1, ν_2, and ν_3, respectively. The lamellar C_nGeQ phases have very similar spectra (29). The last two brands ν_2 and ν_3 are caused by modes within the inner Ge_4Q_6 cage. They are only slightly affected in position and intensity in the C_nMGeQ phases in which the adamantane units are now linked by the metal atoms. The ν_1 modes are caused by the totally symmetric stretching mode associated with the terminal Ge–Q bonds, which are now no longer free. These bands are strongly suppressed or almost disappear. In the region of 380–460 cm^{-1} for C_nMGeS and 230–340 cm^{-1} for C_nMGeSe a broader low-intensity peak occurs that corresponds to the ν_{11} mode.

The adamantane cluster vibrations also dominate the far IR region. Again, comparison with similar compounds supports the integrity of our developed structural model. Figures 14a and 14b show the far IR spectra of the C_{14}ZnGeS and C_{14}ZnGeSe phases, respectively. For example, the C_{14}ZnGeS phase shows the two strongest bands at 405 and 435 cm^{-1}. These bands also occur in $(Me_4N)_4Ge_4S_{10}$ (59) or the lamellar C_nGeS phases (29), but they are now shifted to lower frequencies in our compounds. The intensities, however, vary for different C_nMGeS phases and, in fact, the band at around 400 cm^{-1} is stronger than the one at 435 cm^{-1} in the Zn or Cd compounds while their intensities are almost equal in the Co compound. Similar behavior was

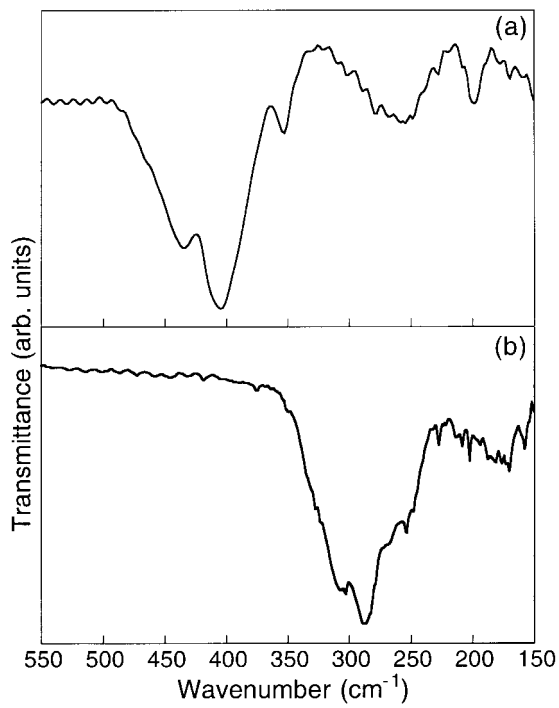

FIG. 14. Far infrared (CsI pellets) spectra of (a) C_{14}ZnGeS and (b) C_{14}CdGeSe.

observed for the Se analogs; the C_{14}GeSe precursor compound for example shows two strong, sharp absorptions at 324 and 282 cm^{-1} with almost equal intensity. The C_nMGeSe phases (M = Zn, Cd; n = 12, 14, 16, 18) have their absorption maximum at ca. 280 cm^{-1}, with a shoulder at around 305 cm^{-1} (60).

The investigation of the mid IR region between 4000 and 600 cm^{-1} gives proof of the presence of the surfactant molecules in all the C_nMGeQ phases. The typical areas for C–H, C–C, and C–N vibrations remain unchanged in position and intensity and correspond to the expected literature values.

Optical Absorption Properties

A major distinction between the silicate or other oxidic mesostructured materials and the chalcogenido materials described here is the considerably more narrow energy band gap of the latter. This makes mesostructured metal chalcogenides potentially interesting for a number of unique applications based on electron and photon processes. Therefore, the optical absorption of the C_nMGeQ compounds was studied with diffuse reflectance solid state UV/vis spectroscopy. The materials are semiconductors and those with d^{10} metals show well-defined sharp optical absorptions associated with bandgap transitions in the energy range 1.4–3.6 eV. By comparison mesostructured silicas have optical energy gaps >7 eV.

Figure 15 shows the electronic absorption spectra of some $C_{14}M$GeQ compounds with M = Zn, Cd, Hg. As expected, the absorption edges for the selenium compounds generally occur at lower energies than those of the corresponding sulfur analogs. Within the same chalcogenide family, the lowest energy absorption edge occurs in the Hg analog. The optical gap transitions most likely involve charge transfer excitations from the top of a valence band composed of predominantly p orbitals of sulfur atoms, to the bottom of a conduction band made mainly from empty s and p type metal orbitals.

The absorption edge for a given C_nMGeQ compound is independent of the C_n surfactant chain length. This is demonstrated in Fig. 16 for the C_nZnGeS and C_nZnGeSe phases with n = 12, 14, 16, and 18. The bandgaps for the sulfide phases lie in a narrow energy range from 3.2 to 3.4 eV, while the corresponding selenide phases have values from 2.3 to 26 eV. When Zn is replaced with Cd the corresponding C_nCdGeSe phases have slightly lower values between 2.1–2.4 eV. The smooth and regular evolution of optical absorption spectra as a function of M and Q is consistent with the fact that we are dealing with a series of structural analogs. That is the metal/Ge/Q connectivities within the framework, an important factor affecting the bandgap values, are very similar throughout the entire C_nMGeQ family.

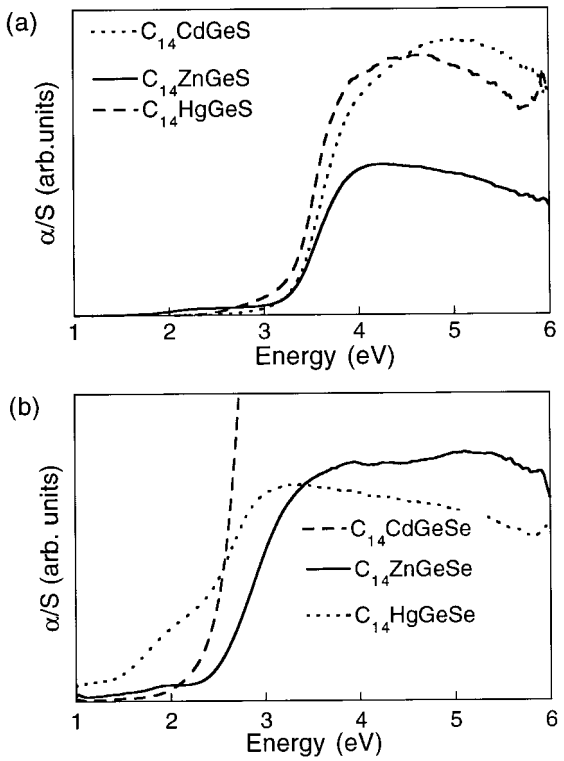

FIG. 15. Optical absorption spectra of $C_{14}M$GeQ with M = Zn, Cd, Hg and (a) Q = S and (b) Q = Se.

The optical spectra of the Co^{2+} compounds are dramatically different from those of the d^{10} metals because of the intense optical charge transfer transitions occurring between the chalcogenide p orbitals and the empty d orbitals of Co^{2+}. These bands occur at 333, 717, and 1741 nm (see Fig. 17). Furthermore, weaker d–d transitions are almost certainly occurring as well, since in a tetrahedral coordination environment they are spectroscopically partially allowed. The spectral pattern observed is similar to those observed for well-known tetrahedral Co^{2+} complexes in which the metal has a full chalcogenide environment (61).

Table 2 summarizes the bandgap values for these and other members of the C_nMGeQ family. For comparison the last row contains the bandgaps of the lamellar C_{14}GeQ precursor phases, which lie at energies higher than those of the corresponding mesostructured C_nMGeQ compounds. The lowest bandgap is found in the Ni analogs with 1.1 and 1.0 eV for C_{16}NiGeS and C_{14}NiGeSe, respectively.

The C_nMGeSe compounds (M = Zn, Cd) are sensitive and turn from yellow or brownish-yellow to red within a few days of air exposure, and after several weeks they become almost black. The members of the series C_nCdGeSe (n = 12, 14, 16, 18), for example, turn from light yellow to red within 4 days. This darkening is due to elemental Se forming on the surface (62).

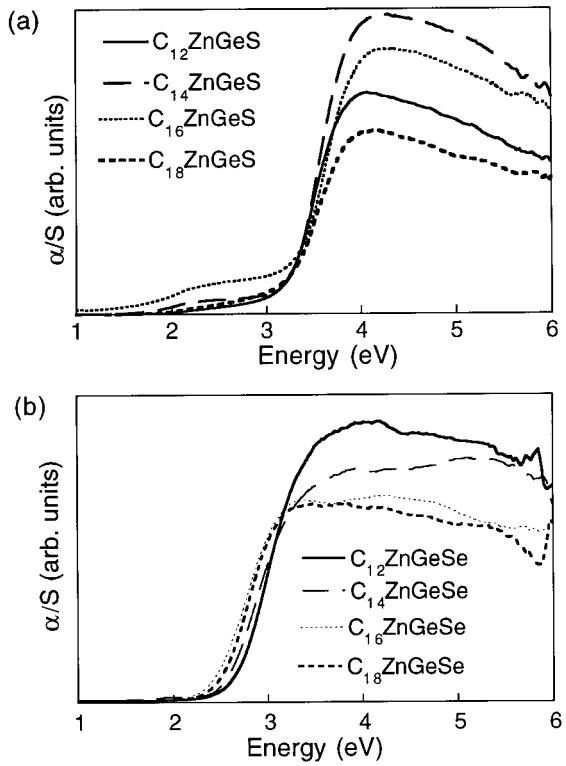

FIG. 16. Optical absorption spectra of (a) C_nZnGeS and (b) $C_nZnGeSe$ ($n = 12, 14, 16, 18$).

Thermal Stability, Calcination, and Adsorption

Thermal gravimetric analyses of the $(R\text{–}NMe_3)_2[MGe_4Q_{10}]$ compounds show no appreciable weight loss up to 150°C. In the range between 150 and 400°C weight loss occurs in a single continuous step, corresponding to the complete removal of surfactant molecules. Unlike the formamide synthesized materials (38), we see no evidence for the presence of water. Figure 18 shows two characteristic TGA curves of $C_{14}CdGeS$ and $C_{14}CdGeSe$. In Table 3 the calculated percentage weight loss and the observed percentage weight loss for the series C_nMGeQ (M = Zn, Cd; Q = S, Se; $n = 12, 14, 16, 18$) are given. It is clear from the table that the measured values correspond to two surfactant molecules per adamantane unit.

TABLE 2
Energy Bandgaps of all Characterized C_nMGeQ Phases

Compound	Bandgaps (eV)	
	Q = S	Q = Se
$C_{14}ZnGeQ$	3.13	2.37
$C_{14}CdGeQ$	3.28	2.20
$C_{14}HgGeQ$	2.89	1.41
$C_{14}CoGeQ$	—	~1.6
$C_{14}NiGeQ$	~1.1	~1.0
$C_{14}GeQ$	3.60	2.72

Note. All compounds reveal values between 2 and 3 eV, which is in the typical semiconductor range.

Combines TGA/mass spectroscopy analysis of the evolved volatile products shows R–NMe_2 and NMe_3 and their decomposition products. The powder XRD patterns of the decomposed materials, obtained at 400–500°C, correspond to amorphous GeS_2 and crystalline MS in the sulfides. In the selenide phases crystalline $GeSe_2$ can be identified as well as MSe in some cases, e.g., ZnSe for C_nMGeSe, from the powder XRD patterns. These observations lead to the formulation of the following equation for decomposition:

$$(R\text{–}NMe_3)_2[MGe_4Q_{10}] \xrightarrow{>200^\circ C} MQ + 4GeQ_2 + NMe_3 + Me_2Q + R\text{–}H + \text{decomp. } R\text{–}H, \text{ etc.} \quad [5]$$

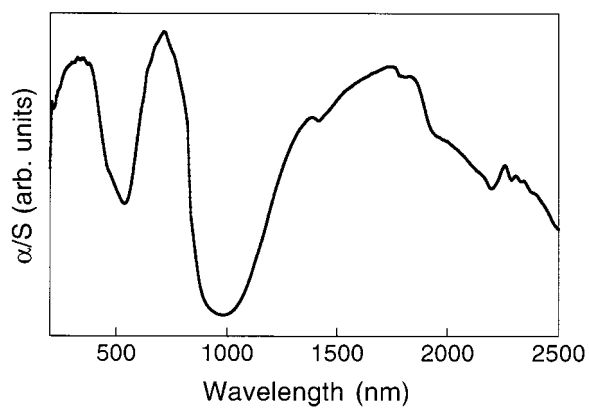

FIG. 17. Optical absorption spectrum of $C_{14}CoGeS$.

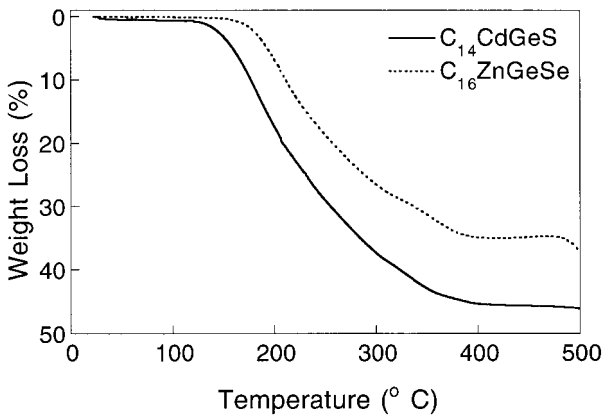

FIG. 18. Thermogravimetric analyses of $C_{14}CdGeS$ and $C_{16}ZnGeSe$; the calculated values correspond to two C_{14} surfactant units per adamantane cluster.

TABLE 3
Observed and Calculated Weight Loss Percentages for the Series of C_nMGeS and C_nMGeSe with $n = 12, 14, 16, 18$ and $M =$ Zn, Cd

	% Weight loss							
	C_{12}		C_{14}		C_{16}		C_{18}	
Compound	Obs.	Cal.	Obs.	Cal.	Obs.	Cal.	Obs.	Cal.
C_nZnGeS	42.1	43.1	43.6	44.7	44.9	45.8	45.1	47.1
$C_nZnGeSe$	29.7	28.5	28.5	30.9	33.9	33.2	28.3	35.3
C_nCdGeS	41.0	41.4	43.5	42.9	43.9	44.1	44.0	45.3
$C_nCdGeSe$	31.7	27.7	30.9	30.1	34.9	32.3	32.3	34.4

Based on the TGA experiments we have attempted to remove the organic component by heat treatment, a step analogous to the air calcination used to remove the surfactant template molecules for micro- and mesoporous oxides. The major difference in the procedure is that the mesostructured chalcogenides were heated under dynamic vacuum and at much lower temperatures than the oxides. We chose "calcination" temperatures at around 180–200°C, typically at the inflection point of the weight loss curves, if observable, or lower. Weight losses vs time curves show that about 70–80% of the organic part can be removed, *without collapse* of the framework, after heating under vacuum for 3–4 days, but most of the reaction is complete after several hours. Again this is in sharp contrast with what was reported for the complete after several hours. Again this is in sharp contrast with what was reported for the $CTA/M_2Ge_4Se_{10}$ systems that lose only 30–40% of their surfactant species at $\sim$300°C (38).

In the "calcined" mesostructured materials the low-angle, high *d*-spacing peak remains prominent in the diffraction pattern, though it shifts slightly to higher angles, indicating a decrease in the mesopore spacing of typically $\sim$3–5 Å. At the same time the high-angle region of the XRD patterns unambiguously shows that the frameworks remain essentially intact with only a slight modification of the shape of the diffuse scattering. This suggests that the structure of the calcined products mirrors that of the precursor $(R\text{–}NMe_3)_2[MGe_4Q_{10}]$ compounds. In fact, a sample that has been calcined appears by TEM to have worm hole, tunnel-like features with widths of 25–35 Å (see Fig. 19) in a fashion similar to that of its precursor discussed above.

We expected the calcined products to adsorb molecules in the empty channel sites created by the evacuation of surfactant molecules and visible by TEM and we investigated the adsorption of N_2, CO_2, and H_2O molecules. No adsorption of N_2 was observed in the sulfides. The Se phases show adsorption isotherms typical of a nonporous material, adsorbing only on the external surfaces of the solid. In this case, the single point surface area calculated from the isotherm is 31 m^2/g at p/p_0 0.25.

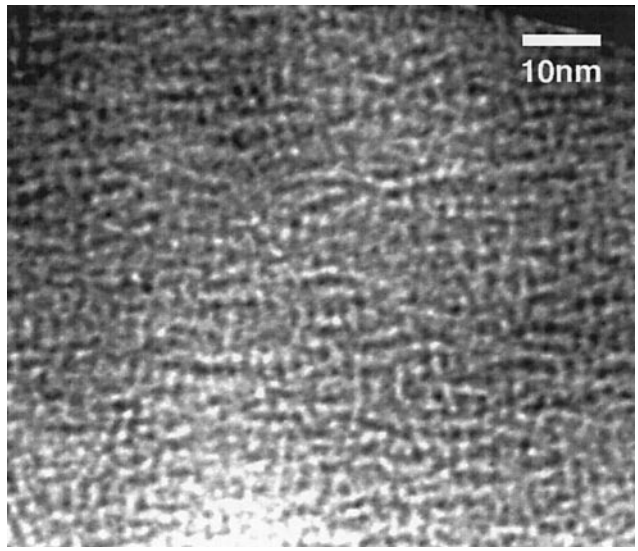

FIG. 19. TEM of calcined C_{16}NiGeS. The pore space is represented in the white regions.

A water adsorption study of calcined C_{14}ZnGeS also shows adsorption mainly on the external surface at higher water pressures and the isotherm is similar to a nonporous material. The most probable cause of this is that the entrances of the channels are constricted or blocked, probably by organic decomposition products created through the anaerobic calcination process. Even after very short calcination times ($\sim$30 min at 180–200°C) blocking could not be prevented. We tried a few experiments to "open" the channels with the treatment of the samples with different acids such as HCl or HNO_3, for example. The result was a partial decomposition of the framework due to oxidation processes, proved by the presence of elemental selenium in the XRD powder patterns, rather than a dissolving process of the material obstructing the channel entrances. A better surfactant removal method needs to be developed in order to unlock the absorption potential of these materials. Interestingly, washing with DMF seems to remove some of the channel blocking impurities and raises the observed surface area from $\sim$31 to $\sim$45 m^2/gr.

CONCLUDING REMARKS

The aqueous reactions of $[Ge_4Q_{10}]^{4-}$ clusters with divalent transition metal ions in the presence of templating surfactants leads to a new family of mesostructured compounds with the general formula $(C_nH_{2n+1}NMe_3)_2[MGe_4Q_{10}]$ (M = Zn, Cd, Hg, Co; Q = S, Se; n = 12, 14, 16, 18). These materials possess a disordered three-dimensional framework structure $^3_\infty[MGe_4Q_{10}^{2-}]$ in which the adamantane clusters are the basic building blocks. The surfactant

molecules occupy hereby the tunnels, which crisscross this framework in a disordered worm hole-like manner. Only short-range local order exists in the covalent framework. The diameter of the wormholes is tunable with the provided surfactant molecule and range between 22 and 32 Å. Raman and infrared spectroscopic investigations also confirm the integrity of the adamantane clusters within the framework structure. All compounds are wide bandgap semiconductors, with the Se phases showing values generally lower than those of the sulfide analogs. The compounds lose up to 80% of their surfactant molecules when heated up anaerobically to 250°C without framework collapse. However, the surfactant removal levels a channel-blocking residue that prevents access. Current investigations focus on new ways to remove the surfactant molecules, exploration of new surfactant species, and experimentation with nonaqueous solvents. Structures of this type may be potentially interesting for specialized applications such as in shape selective catalysis, electro- and photocatalysis, environmental remediation of heavy metals, and chemoselective sensing.

ACKNOWLEDGMENTS

Financial support from the National Science Foundation CHE 99-03706, (Chemistry Research Group) is gratefully acknowledged. This work made use of the SEM and TEM facilities of the Center for Electron Optics, Michigan State University. We acknowledge the use of the W. M. Keck Microfabrication Facility at Michigan State University, which is a NSF MRSEC facility. We thank Professor T. J. Pinnavaia for fruitful discussions. M.W. thanks the Deutsche Forschungsgemeinschaft for a postdoctoral research fellowship.

REFERENCES

1. C. L. Bowes and G. A. Ozin, *Adv. Mater.* **8,** 13 (1996); (b) G. A. Ozin, *Adv. Mater.* **7,** 335 (1995); (c) G. A. Ozin, *Adv. Mater.* **4,** 612 (1992).
2. J. B. Parise, *Science* **251,** 293 (1991); (b) H. Ahari, C. L. Bowes, T. Jiang, T. Lough, A. Lough, G. A. Ozin, R. L. Bedard, S. Petrov, and D. Young, *Adv. Mater.* **7,** 375 (1995); (c) J. B. Parise, Y. Ko, J. Rijssenbeek, D. M. Nellis, K. Tan, and S. Koch, *J. Chem. Soc. Chem. Commun.* 527 (1994).
3. (a) J. Grimblot, *Catal. Today* **41,** 111 (1998); (b) I. M. Schewemiller, K. F. Koo, M. Columbia, F. Li, and G. L. Schrader, *Chem Mater.* **6,** 2327 (1994); (c) E. P. S. Barrett, A. J. Blackburn, M. A. Yates, Y. Wang, and P. A. Sermon, *Stud. Surf. Sci. Catal.* **77,** 207 (1993).
4. (a) D. Cahen, L. Chernyak, K. Gartsman, I. Lyubomirsky, and R. Triboulet, *Jpn. J. Appl. Phys.* **32,** 660 (1993); (b) D. Cachen, J. M. Gilet, C. Schmitz, L. Chernyak, K. Gartsman, and A. Jakubowicz, *Science* **258,** 271 (1992); (c) J. Lai, L. Cai, and D. L. Morel, *Appl. Phys. Lett.* **59,** 1990 (1991); (d) P. B. Atanackovic, T. A. Steele, and J. Munch, *IEEE J. Quantum Elect.* **33,** 393 (1997); (e) H. D. Abruna and A. J. Bard, *J. Electrochem. Soc.* **129,** 673 (1982); (h) H. S. White, F. R. F. Fan, and A. J. Bard, *J. Electrochem. Soc.* **128,** 1045 (1981).
5. (a) I. E. Ture, G. J. Russell, and J. Woods, *J. Cryst. Growth* **59,** 223 (1982); (b) H. W. Willemsen, P. J. Scanlon, F. R. Shepherd, and W. D. Westwood, *J. Electrochem. Soc.* **127,** C398 (1980); (c) S. R. Jawalekar, and M. K. Rao, *Int. J. Electron.* **46,** 483 (1979); (d) N. V. Joshi and S. Swanson, *Solid State Electron.* **30,** 105 (1987); (e) J. Stankiewicz and M. Dilorenzo, *J. Appl. Phys.* **69,** 1479 (1991); (f) J. Vaitkus, R. Tomasiunaś, and J. Kutra, *J. Cryst. Growth.* **101,** 826 (1990); (g) S. Bhushan, and L. C. Giriya, *Crystal. Res. Technol.* **23,** 919 (1988); (h) C. Schmidt and H. Haeuseler, *Mater. Res. Bull.* **30,** 585 (1995).
6. (a) K. Meeker and A. B. Ellis, *J. Phys. Chem. B* **103,** 995 (1999); (b) H. E. Ruda, *Science* **283,** 646 (1999).
7. R. L. Bedard, S. T. Wilson, L. D. Vail, E. M. Bennett, and E. M. Flanigen, Zeolites: Facts, Figures, Future P. A. Jacobs, R. A. van Santen, (Eds.), p. 375. Elsevier Science, Amsterdam, The Netherlands, 1989.
8. R. L. Bedard, L. D. Vail, S. T. Wilson, and E. M. Flanigen, *U.S. Patent* 4,880,761, 1989.
9. O. M. Yaghi, Z. Sun, D. A. Richardson, and T. L. Groy, *J. Am. Chem. Soc.* **116,** 807 (1994).
10. C. L. Cahill and J. B. Parise, *Chem. Mater.* **9,** 807 (1997).
11. J. B. Parise and K. M. Tan, *J. Chem. Soc. Chem. Commun.* **527,** 1687 (1996).
12. (a) C. L. Bowes, A. J. Lough, A. Malek, G. A. Ozin, S. Petrov, and D. Young, *Chem. Ber.* **129,** 283 (1996); (b) H. Ahari, A. Garcia, S. Kirkby, G. A. Ozin, D. Young, and A. J. Lough, *J. Chem. Soc. Dalton Trans.* 2023 (1998).
13. C. L. Bowes, W. U. Huynh, S. J. Kirkby, A. Malek, G. A. Ozin, S. Petrov, M. Twardowski, D. Young, R. L. Bedard, and R. Broach, *Chem. Mater.* **8,** 2147 (1996).
14. S. Dhingra and M. G. Kanatzidis, *Science* **258,** 1769 (1992).
15. K.-W. Kim and M. G. Kanatzidis, *J. Am. Chem. Soc.* **114,** 4878 (1992).
16. K.-W. Kim and M. G. Kanatzidis, *J. Am. Chem. Soc.* **120,** 8124 (1998).
17. (a) C. L. Bowes, S. Petrov, G. Vork, D. Young, G. A. Ozin, and R. L. Bedard, *J. Mater. Chem.* **8,** 711 (1998); (b) T. Jiang, A. Lough, and G. A. Ozin, *Adv. Mater.* **10,** 42 (1998); (c) T. Jiang, A. Lough, G. A. Ozin, R. L. Bedard, and R. Broach, *J. Mater. Chem.* **8,** 721 (1998); (d) T. Jiang, A. Lough, G. A. Ozin, D. Young, and R. L. Bedard, *Chem. Mater.* **7,** 245 (1995); (e) H. Ahari, G. A. Ozin, R. L. Bedard, S. Petrov, and D. Young, *Adv. Mater.* **7,** 370 (1995); (f) T. Jiang, G. A. Ozin, and R. L. Bedard, *Adv. Mater.* **6,** 860 (1994).
18. (a) W. S. Sheldrick, and H.-G. Braunbeck, *Z. Naturforsch. B.* **45,** 1643 (1990); (b) W. S. Sheldrick, H.-G. Braunbeck, *Z. Anorg. Allg. Chem.* **619,** 1300 (1993); (c) J. B. Parise, Y. Ko, J. Rijssenbeek, D. M. Nellis, K. Tan, and S. Koch, *J. Chem. Soc. Chem. Commun.* 527 (1994).
19. (a) P. Enzel, G. S. Henderson, G. A. Ozin, and R. L. Bedard, *Adv. Mater.* **7,** 64 (1995); (b) T. Jiang, A. J. Lough, G. A. Ozin, and D. Young, *Chem. Mater.* **7,** 245 (1995).
20. Y. Ko, K. Tan, D. M. Nellis, S. Koch, and J. B. Parise, *J. Solid State Chem.* **114,** 506 (1995).
21. G. A. Marking and M. G. Kanatzidis, *Chem. Mater.* **7,** 1915 (1995).
22. (a) T. J. McCarthy, T. A. Tanzer, and M. G. Kanatzidis, *J. Am. Chem. Soc.* **117,** 1294 (1995); (b) K. Chondroudis, and M. G. Kanatzidis, *J. Solid State Chem.* **136,** 328 (1998).
23. K.-W. Kim and M. G. Kanatzidis, *Inorg. Chem.* **30,** 1966 (1991).
24. (a) W. S. Sheldrick and M. Wachhold, *Angew. Chem. Int. Ed. Engl.* **36,** 206 (1997) (b) M. G. Kanatzidis, and S.-P. Huang, *Coord. Chem. Rev.* **130,** 509 (1994); (c) G. W. Drake and J. W. Kolis, *Coord. Chem. Rev.* **137,** 131 (1994); (d) W. S. Sheldrick and M. Wachhold, *Coord. Chem. Rev.* **176,** 211 (1998).
25. (a) T. Jiang, G. A. Ozin, A. Verma, and R. L. Bedard, *J. Mater. Chem.* **8,** 1649 (1998); (b) C. L. Bowes, S. Petrov, G. Vovk, D. Young, G. A. Ozin, and R. L. Bedard, *J. Mater. Chem.* **8,** 711 (1998).
26. (a) C. T. Kresge, M. E. Leonowicz, W. J. Roth, J. C. Vartuli, and J. S. Beck, *Nature* **359,** 710 (1992); (b) J. S. Beck, J. C. Vartuli, W. J. Roth, M. E. Leonowicz, C. T. Kresge, K. D. Schmitt, C. T.-W. Chu, D. H. Olson, E. W. Sheppard, S. B. McCullen, J. B. Higgins, J. L. Schlenker, *J. Am. Chem. Soc.* **114,** 10834 (1992); (c) A. Sayari, and P. Liu, *Microporous Mater.* **12,** 149 (1997).

27. (a) P. T. Tanev, and T. J. Pinnavaia, *Science* **271,** 1267 (1996); (b) P. T. Tanev and T. J. Pinnavaia, *Science* **267,** 865 (1995); (c) P. T. Tanev, M. Chibwe, and T. J. Pinnavaia, *Nature* **368,** 321 (1994).
28. B. Krebs, *Angew. Chem. Int. Ed. Engl.* **22,** 113 (1983).
29. F. Bonhomme, M. G. Kanatzidis, *Chem. Mater.* **10,** 1153 (1998).
30. M. J. MacLachlan, S. Petrov, R. L. Bedard, I. Manners, and G. A. Ozin, *Angew.. Chem. Int. Ed. Engl.* **37,** 2076 (1998).
31. (a) V. Tohver, P. V. Braun, M. U. Pralle, and S. I. Stupp, *Chem. Mater.* **9,** 1495 (1997); (b) P. Osenar, P. V. Braun, and S. I. Stupp, *Adv. Mater.* **8,** 1022 (1996).
32. (a) P. V. Braun, P. Osenar, and S. I. Stupp, *Nature* **380,** 325 (1996); (b) S. I. Stupp, and P. V. Braun, *Science* **277,** 1242 (1997).
33. J. Li, H. Kessler, M. Soulard, L. Khouchaf, and M.-H. Tuiler, *Adv. Mater.* **10,** 946 (1998).
34. (a) T. Jiang and G. A. Ozin, *J. Mater. Chem.* **8,** 1099 (1998). (b) T. Jiang, G. A. Ozin, and R. L. Bedard, *J. Mater. Chem.* **8,** 1641 (1998).
35. (a) J. Q. Li and H. Kessler, *Microporous Mater.* **9,** 141 (1997); (b) J. Q. Li, H. Kessler, and L. Delmotte, *J. Chem. Soc. Faraday Trans.* **93,** 665 (1997); (c) J. Q. Li, L. Delmotte, and H. Kessler, *J. Chem. Soc. Chem. Commun.* 1023 (1996).
36. M. Fröba, and N. Oberender, *J. Chem. Soc. Chem. Commun.* 1729, (1997).
37. (a) R. Bissessur, J. Heising, W. Hirpo and M. G. Kanatzidis, *Chem. Mater.* **8,** 318 (1996); (b) J. Brenner, C. L. Marshall, L. Ellis, N. Tomczyk, J. Heising, and M. G. Kanatzidis, *Chem. Mater.* **10,** 1244 (1998); (c) J. Heising, F. Bonhomme, and M. G. Kanatzidis, *J. Solid State Chem.* **139,** 22 (1998).
38. (a) M. J. MacLachlan, N. Coombs, and G. A. Ozin, *Nature* **397,** 681 (1999). (b) M. J. MacLachlan, N. Coombs, R. L. Bedard, S. White, L. K. Thompson, and G. A. Ozin, *J. Am. Chem. Soc.* **121,** 12005 (1999).
39. H. Klug, and L. Alexander, "X-Ray Diffraction Procedures for Polycrystalline and Amorphous Materials," Wiley. New York, 1974.
40. B. E. Warren, "X-Ray Diffraction," Dover; New York, 1990.
41. Egami, T. *Mater. Trans. JIM* **31,** 163 (1990).
42. S. J. L. Billinge and T. Egami, *Phys. Rev. B* **47,** 14386 (1993).
43. T. J. McCarthy, S.-P. Ngeyi, J.-H. Liao, D. C. DeGroot, T. Hogan, C. R. Kannewurf, and M. G. Kanatzidis, *Chem. Mater.* **5,** 331 (1993).
44. Further studies involving other metal ions such as Mn^{2+}, Sn^{2+}, and In^{3+} will be reported elsewhere.
45. K. K. Rangan, S. J. L. Billinge, V. Petkov, J. Heising, and M. G. Kanatzidis, *Chem. Mater.* **11,** 2629 (1999).
47. K. G. Severin, T. M. Abdel-Fattah, and T. J. Pinnavaia, *Chem. Commun.* 1471 (1998).
48. (a) E. Prouzet and T. J. Pinnavaia *Angew. Chem. Int. Ed. Engl.* **36,** 516 (1997); (b) W. Z. Zhang, T. R. Pauly, and T. J. Pinnavaia, *Chem. Mater.* **9,** 2491 (1997); (c) P. T. Tanev and T. J. Pinnavaia, *Chem. Mater.* **8,** 2068 (1996); (d) S. A. Bagshaw and T. J. Pinnavaia, *Angew. Chem. Int. Ed. Engl.* **35,** 1102 (1996).
49. S. A. Bagshaw, E. Prouzet, and T. J. Pinnavaia, *Science* **269,** 1242 (1995).
50. S. J. L. Billinge, V. Petkov, M. F. Thorpe, M. Lei, M. Wachhold, K. K. Rangan, and M. G. Kanatzidis, in preparation.
51. (a) O. Achak, J. Y. Pivan, M. Maunaye, M. Louër, and D. Louër, *J. Alloys Compd.* **219,** 111 (1995); (b) O. Achak, J. Y. Pivan, M. Maunaye, M. Louër, and D. Louër, *J. Solid State Chem.* **121,** 473 (1996).
52. S. J. L. Billinge, *in* "Local Structure from Diffraction" (M. Thorpe and S. J. L. Billinge, Eds.), Plenum, New York, 1998.
53. K. K. Rangan, M. Wachhold, V. Petkov, S. J. L. Billinge, and M. G. Kanatzidis, unpublished results.
54. Structure parameters used for the calculations of the X-Ray diffraction powder patterns of the amorphous C_nCdGeS framework: Ge–S_b 2.246 Å, Ge–S_t 2.173 Å, Cd–S bond range 2.48–2.66 Å, with a probability maximum at 2.51 Å, S–Cd–S angle: average 109.5°, narrow range 95–145°, wide range 73–173°, Ge–S_t–Cd angle: average 113°, narrow range 97–120°, wide range 85–142°. Distance from the center of the Ge_4S_{10} unit to the terminal S atom: 4.419 Å.
55. N. Mousseau and L. J. Lewis, *Phys. Rev. Lett.* **78,** 1484 (1997).
56. The construction of amorphous networks with tetrahedral topology and only even-membered rings is a very challenging task and the subject of great theoretical investigations. Also see, G. A. N. Connell and R. J. Temkin, *Phys. Rev. B.* **9,** 5323 (1974).
57. M. F. Thorpe and M. Lei, work in progress.
58. J. Campbell, D. P. DiCiommo, H. P. A. Mercier, A. M. Pirani, G. J. Schrobilgen, and M. Willuhn, *Inog. Chem.* **34,** 6265 (1995).
59. J. Y. Pivan, O. Achak, M. Louër, and D. Louër, *Chem. Mater.* **6,** 827 (1994).
60. The spectra of the far IR region can rather serve as a fingerprint area for certain members of a C_nMGeQ family regardless of the surfactant chain length. The phases have a very characteristic vibrational pattern in the range 120–380 cm^{-1}. Only minor differences in the patterns of the corresponding Cd phases are recognizable; however, they reveal a characteristic fingerprint for each family of compounds with different surfactant chains but the same metal *M* and chalcogen *Q*.
61. I. G. Dance, *J. Am. Chem. Soc.* **101,** 6264 (1979).
62. The absorption edge red shifts by a significant $\sim$0.5 eV which is independent of the surfactant species. XRD spectra show that a small amount of elemental Se is now present, presumably responsible for the reddish (and later black) darkening of the samples. The apparent bandgaps for all air-exposed C_nMGeSe ($n = 12, 14, 16, 18$; M = Zn, Cd) phases have values of ca. 1.8 eV after 4 days, whereas the value for black selenium is 1.6 eV. The formation of Se seems to be on the surface of the particles because the frameworks appear to be intact, as shown by the retention of the low-angle peak and the diffuse scattering in the XRD powder patterns. Treatment of C_nMGeSe with *tri-n*-butylphosphine, which is well known to react with elemental Se to form *tri-n*-butylphosphine-selenide, leads to an immediate return to the original color. Furthermore, if the air-exposed, red samples are ground again, the color changes almost to the original tone. These observations suggest that the Se forms due to surface oxidation and does not reside in the interior of the framework. Interestingly, the surface decomposition process to form Se can be accelerated by X-ray exposure of the samples. In this case the conversion to a red product with the same red shift is completed within a few hours.